On a dark-field signal generated by micrometer-sized calcifications in phase-contrast mammography

On a dark-field signal generated by micrometer-sized calcifications in phase-contrast mammography

Thilo Michel[1]**, Jens Rieger**[1]**, Gisela Anton**[1]**, Florian Bayer**[1]**,
Matthias W Beckmann**[2]**, Jürgen Durst**[1]**, Peter A Fasching**[2,3]**,
Wilhelm Haas**[4]**, Arndt Hartmann**[2]**, Georg Pelzer**[1]**, Marcus Radicke**[5]**,
Claudia Rauh**[2]**, André Ritter**[1]**, Peter Sievers**[6,1]**,
Rüdiger Schulz-Wendtland**[7]**, Michael Uder**[7]**, David L Wachter**[8]**,
Thomas Weber**[1]**, Evelyn Wenkel**[7]** and Andrea Zang**[1]

[1] Erlangen Centre for Astroparticle Physics (ECAP), Friedrich-Alexander-Universität
Erlangen-Nürnberg, Erwin-Rommel-Str 1, D-91058 Erlangen, Germany
[2] Department of Gynecology and Obstetrics, University Hospital Erlangen,
Friedrich-Alexander-Universität Erlangen-Nürnberg, Universitätsstr 21-23, D-91054 Erlangen,
Germany
[3] Division of Hematology/Oncology, David Geffen School of Medicine, University of California
at Los Angeles, 10833 Le Conte Avenue, Los Angeles, CA, USA
[4] Pattern Recognition Lab, Friedrich-Alexander-Universität Erlangen-Nürnberg, Martensstr 3,
D-91058 Erlangen, Germany
[5] Siemens AG Healthcare Sector, Henkestr 127, D-91052 Erlangen, Germany
[6] Physikalisch-Technische Bundesanstalt (PTB), Bundesallee 100, D-38116 Braunschweig,
Germany
[7] Institute of Diagnostic Radiology, University Hospital Erlangen,
Friedrich-Alexander-Universität Erlangen-Nürnberg, Maximiliansplatz 2, D-91054 Erlangen,
Germany
[8] Institute of Pathology, University Hospital Erlangen, Friedrich-Alexander-Universität
Erlangen-Nürnberg, Krankenhausstr 12, D-91054 Erlangen, Germany

E-mail: Thilo.Michel@physik.uni-erlangen.de

Abstract
We show that a distribution of micrometer-sized calcifications in the human
breast which are not visible in clinical x-ray mammography at diagnostic dose
levels can produce a significant dark-field signal in a grating-based x-ray phase-
contrast imaging setup with a tungsten anode x-ray tube operated at 40 kVp. A
breast specimen with invasive ductal carcinoma was investigated immediately
after surgery by Talbot–Lau x-ray interferometry with a design energy of
25 keV. The sample contained two tumors which were visible in ultrasound
and contrast-agent enhanced MRI but invisible in clinical x-ray mammography,
in specimen radiography and in the attenuation images obtained with the
Talbot–Lau interferometer. One of the tumors produced significant dark-field
contrast with an exposure of 0.85 mGy air-kerma. Staining of histological
slices revealed sparsely distributed grains of calcium phosphate with sizes
varying between 1 and 40 μm in the region of this tumor. By combining the

histological investigations with an x-ray wave-field simulation we demonstrate that a corresponding distribution of grains of calcium phosphate in the form of hydroxylapatite has the ability to produce a dark-field signal which would—to a substantial degree—explain the measured dark-field image. Thus we have found the appearance of new information (compared to attenuation and differential phase images) in the dark-field image. The second tumor in the same sample did not contain a significant fraction of these very fine calcification grains and was invisible in the dark-field image. We conclude that some tumors which are invisible in x-ray absorption mammography might be detected in the x-ray dark-field image at tolerable dose levels.

(Some figures may appear in colour only in the online journal)

1. Introduction

Since Pfeiffer *et al* (2006) have introduced grating-based hard x-ray Talbot–Lau interferometry in combination with standard x-ray tubes, phase-contrast imaging has steadily gained interest in medical physics. Of special interest is the ability to obtain images of the refractive index decrement δ of the object's complex refractive index $n = 1 - \delta + i\beta$ which leads to phase shifts of the traversing x-ray waves. There is hope that soft-tissue contrast could be enhanced compared to attenuation radiography at still acceptable dose exposures. Furthermore, there are substances which, for a given energy, do not show attenuation contrast but show phase-contrast or vice versa (Herzen *et al* 2009).

The differential phase signal is produced at boundaries between tissues with differences in the product of object length and the real part of the refractive index traversed by neighboring x-rays. Accordingly, the method has its strength in applications where high spatial resolution is achieved. Thus, digital mammography is a natural candidate application in medical imaging to be investigated. In digital mammography, typically gadoliniumoxysulfide (Gd_2O_2S), structured CsI(Tl) scintillation detectors, or amorphous Selenium semiconductor detectors with pixel sizes of typically 50–100 μm (Schulz-Wendtland *et al* 2009) are employed. The spectrum of photon energies, typically produced with molybdenum anode or tungsten anode with rhodium filtration at tube voltages below 40 keV, is softer than the spectrum used in other radiography modalities. These rather low photon energies put less stringent requirements on the source grating G0 and analyzer grating G2 of the Talbot–Lau set-up. Additionally, the phase-shifts at borders and thus variations on the wavefront structure are larger at lower energies, which leads to higher sensitivity in the differential phase image and in the dark-field image.

Mammography has been the modality of interest in early work on exploitation of phase-shifting effects in human tissue. Before it had been demonstrated that phase-contrast can be used for imaging in combination with standard x-ray tubes, synchrotron radiation has been used to analyze first tissue-samples as it has been presented in Arfelli *et al* (2000), Kiss *et al* (2004), Ando *et al* (2005), Keyriläinen *et al* (2005). Research in mammography with synchrotron radiation is still continuing (Castelli *et al* 2011). However, grating-based phase-contrast imaging with x-ray tubes for breast cancer diagnosis—like it was described for the first time with full-breast mastectomies in Stampanoni *et al* (2011)—has seen increased interest for practical reasons.

Stampanoni *et al* (2011) have investigated several full breast mastectomies with breast cancer with respect to attenuation, differential phase, and dark-field signals with grating-based

phase-contrast x-ray imaging. In their samples the attenuation image contained the highest contrast. Attenuation, differential phase and the dark-field images were combined using color codes to enhance the visibility of structures. No special structures which are invisible in the attenuation image have been observed in the dark-field image. In contrast to this, Endo *et al* (2011) have reported the occurrence of dark-field signatures in mastectomy samples embedded in formalin. They observed a correlation of the dark-field signal with the histological image containing calcifications. It remains unclear whether these dark-field signals would also have been visible in freshly dissected breast mastectomy samples.

It has already been pointed out by Pfeiffer *et al* (2008), Cong *et al* (2011) and Rigon *et al* (2007) that the dark-field image represents a measure of the ultra small-angle-scattering strength of materials which results in variations of the wavefront structure on a scale smaller than the pixel size (Yashiro *et al* 2010, Lynch *et al* 2011, Malecki *et al* 2012). The dark-field signal is sensitive to electron density variations on microscopic scales in the object. Due to the fact that the ratio between surface and volume of any object increases with decreasing size the hope arises that the dark-field image should offer the possibility to detect distributions of tiny calcifications embedded in breast tissue already at substantially lower concentrations than in attenuation mammography.

We have already observed strong dark-field signals in an earlier work where we investigated six mastectomies of human breast (Anton *et al* 2013). In this previous study we did not perform a quantitative analysis of the origin of the dark-field contrast. In order to gain physical information on the sample and to draw more solid conclusions on the possible origin of dark-field signal we performed a quantitative investigation on a new sample. The sample contained two invasive ductal carcinomas of grades G1 (tumor A) and G2 (tumor B) in the modified Bloom Richardson Elston grading system. Grade G1 describes a well differentiated, G2 a moderately differentiated and G3 (not present in this sample) a poorly differentiated tumor. The sample was one out of six samples with breast cancer in which we have found signals in the dark-field whereas no attenuation or differential phase signals in the same region have been observed. In another six samples with breast cancer no signal above background in the dark-field image has been found. The sample investigated here has been chosen for detailed analysis because the tumors were marked for surgery with guide wires so that correlating the standard mammography images with images obtained with the Talbot–Lau interferometer was secure.

2. Experimental setup

A three-grating x-ray Talbot–Lau interferometer was set up. A standard x-ray tube with tungsten anode (MEGALIX CatPlus 125/40/90, Siemens AG, Erlangen, Germany) with a nominal focal spot size of 0.4 (IEC 60336)—which is equivalent to maximum dimensions of $0.6 \, \text{mm} \times 0.85 \, \text{mm}$—was used at a tube voltage of 40 kV. The distance from the focal spot to the first grating G0 was 166 mm. All gratings had a duty cycle of 50% and have been produced by the Karlsruhe Institute of Technology applying the LIGA process (Kenntner *et al* 2012). The gold source grating G0 had a period of $p_0 = 24.39 \, \mu\text{m}$ and a grating-bar thickness of $150 \, \mu\text{m}$ in the beam direction. The sample was positioned without compression between two 3 mm thick PMMA plates. The center of the object was placed 1438 mm from G0, the π-shifting phase grating G1 was placed at a distance of 64 mm behind the center of the object. G1 had a period of $p_1 = 4.37 \, \mu\text{m}$. The distance between the phase grating G1 and the analyzer grating G2 was 159 mm, which is 3.3 times the first fractional Talbot-distance (plane wave) $d_T = p_1^2/8/\lambda_{\text{design}}$ for the design energy $E_{\text{design}} = hc/\lambda_{\text{design}} = 25 \, \text{keV}$. The distance between the object and the integrating CsI(Tl) flat panel detector was 852 mm. This geometry resulted
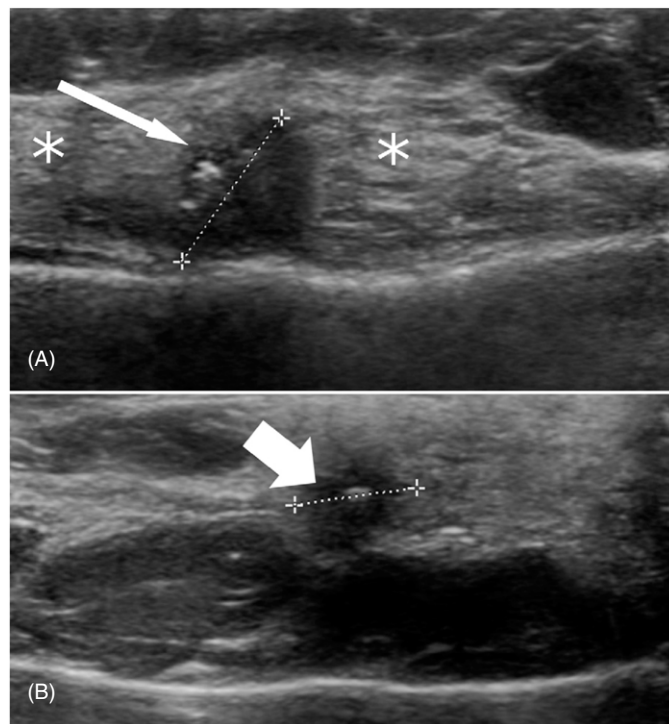
Figure 1. Sonographies: hypoechoic tumor A (long white arrow) and B (short white arrow) within normal hyperechoic breast tissue (asterisk).

in a magnification of the sample by a factor of 1.53. The nickel phase grating G1 comprised grating bars with a thickness of $8.7\,\mu$m in the beam direction, resulting in a design energy of 25 keV for the interferometer. The gold analyzer-grating G2 had a period of $p_2 = 2.4\,\mu$m and a thickness of the grating bars of $100\,\mu$m in beam direction. All gratings were supported by a silicon wafer of 0.5 mm thickness. The flat-panel imaging detector was a Varian PaxScan 2520D with a $600\,\mu$m thick structured CsI(Tl) scintillation layer and $127\,\mu$m physical pixel size.

The digital mammographic images before and after surgery were produced with a MAMMOMAT Inspiration (Siemens AG, Erlangen) with a physical pixel size of $85\,\mu$m. The contrast-agent-enhanced magnetic resonance imaging (MRI) images were obtained with a 1.5 T MAGNETOM Avanto (Siemens AG, Erlangen).

3. Sample analysis

This study has been approved by the ethics committee of the University Hospital Erlangen in the medical faculty of the Friedrich-Alexander-Universität Erlangen-Nürnberg. Written informed consent has been obtained from the patient.

We report the case of a 56-year-old woman who was referred to a certified university breast center for further work-up of a sonographically unclear lesion in the left breast. The woman had no prior breast surgery, did not take any medication and had no serious prior medical condition. The family history was negative for breast cancer. The clinical examination and mammography revealed no suspicious finding. Sonography (figure 1) showed two suspicious hypoechoic, oval
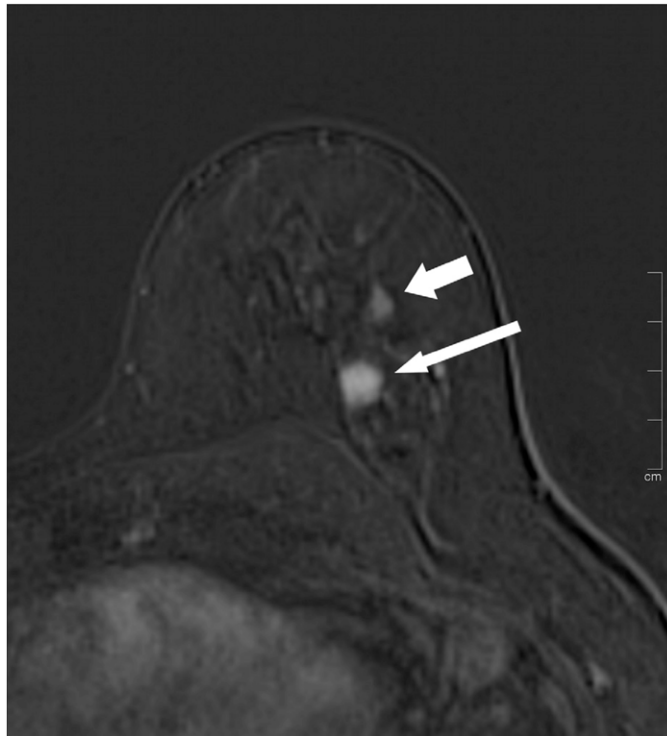
Figure 2. MRI: T1 weighted subtraction MR image of the left breast after intravenous contrast-agent application in axial projection (slice thickness 2.5 mm, sequence: T1 weighted 3D fast low angle shot, TR 7.24 ms, TE 2.38 ms). The long white arrow points at lesion A, the short white arrow at lesion B.

to round lesions in the upper outer quadrant of the left breast with no circumscribed margins and a size of about 9 mm (tumor A) and 6 mm (tumor B). The contrast-agent-enhanced MRI exam (figure 2) on the 1.5 T scanner also showed two suspicious contrast-enhancing lesions in the upper outer quadrant of the left breast with irregular margins with a size of about 9 mm (tumor A) and 7 mm (tumor B). These two lesions correspond to the ones seen on sonography. Histology of the two lesions was verified by sonographically guided core needle biopsies. It revealed invasive ductal carcinoma in both lesions. Both lesions were sonographically marked preoperatively with guide wires followed by mammography in craniocaudal (cc) and mediolateral (ml) projection before surgery.

Presurgical mammography was performed on a MAMMOMAT Inspiration (Siemens AG, Erlangen, Germany), using tungsten as anode target material, and rhodium as filter material. The presurgical mammographies were acquired with a focal spot size smaller than 0.45 mm × 0.45 mm (0.3 following IEC 60336), in cc projection with 29 kV, 93 mAs, and compression force 71.4 N; and in ml projection with 28 kV, 83 mAs, and compression force 78.3 N. In cc projection the air kerma amounted to 3.18 mGy, in ml projection to 2.5 mGy. No tumor is visible in conventional mammography (figure 3).

The lumpectomy breast tissue 6.5 cm × 5.5 cm × 2.1 cm was dissected in six slices with differing thicknesses. Dissected slice number 3 (approximately 5 mm thick) with parts of the two tumors and two guide wires (figure 4) underwent specimen radiography. The radiography was performed at 26 kV (15 mAs) on a Siemens MAMMOMAT Inspiration using magnification mode with a focal spot size smaller than 0.15 mm × 0.15 mm (0.1 following
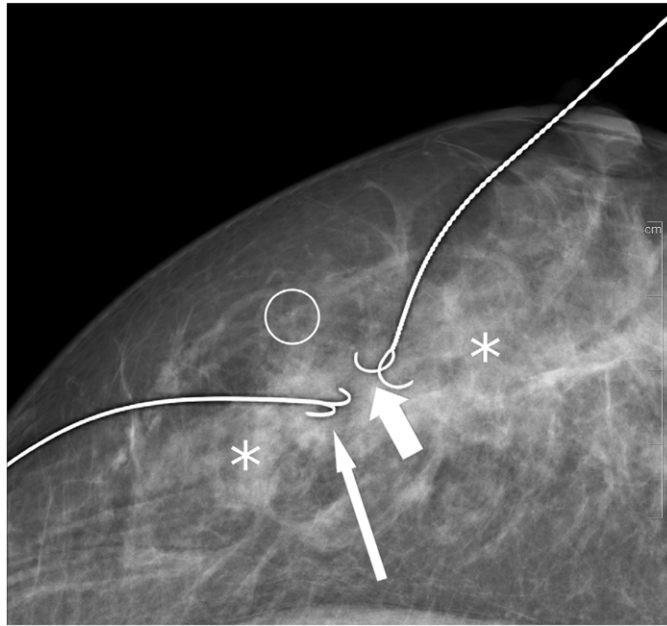
Figure 3. Detail of the conventional mammography in cc projection just before surgery: no tumor margin nor obvious suspicious microcalcifications are seen on conventional mammography. The smooth wire is directly placed in the center of tumor A (long white arrow) with its needle tips. The twisted wire is directly placed in the center of tumor B (short white arrow) with its needle tips. A few microcalcifications in surrounding tissue (circle) are visible. Asterisk: normal hyperdense fibroglandular tissue.

IEC 60336) on tungsten anode with rhodium filtration without compression. The air kerma applied was 0.66 mGy. No tumor is visible in specimen radiography (figure 4). Post-surgical histology confirmed the diagnosis of two lesions.

The subsequent measurements with the Talbot–Lau x-ray interferometer have been performed with slice 3 which contained the guide wires and parts of the two tumors. The results are described in detail in section 4. In the following, sample always refers to slice 3.

After the interferometric measurements the sample has been embedded in paraffin. A microtome cut histological section has been stained using von Kossa stain which is sensitive to the phosphate in calcium phosphate. The stained histological section was scanned with a microscope. Figure 5 shows the von Kossa-stained histological section with the region of tumor A (tumor B, normal breast tissue) marked by a red (blue, green) rectangle. Figures 6–9 show microscope images of these regions with a higher magnification. Histological examination of a large section slide revealed breast tissue with two separate invasive carcinomas on the same slide as well as an *in-situ* component consisting of a 3.3 cm low-grade DCIS (ductal carcinoma *in situ*) without necrosis and only sparse microcalcifications (figure 5). Invasive tumor A represented a well-differentiated invasive tubular carcinoma and measured 0.7 cm. This carcinoma showed numerous microcalcifications (calcium phosphate) with sizes from 1 to 40 micrometers (figures 6 and 7) which were predominantly located intraluminal and at the basal membranes. Invasive tumor B was a moderately differentiated invasive ductal carcinoma of no special type with a more solid growth pattern, and it revealed only sparse microcalcifications measuring 3–6 micrometers, primarily located at the basal membranes (figure 8). Tumor A exhibited a more prominent desmoplastic stromal response whereas the infiltrated fatty tissue in tumor B showed only a minor reaction. Taken together, the
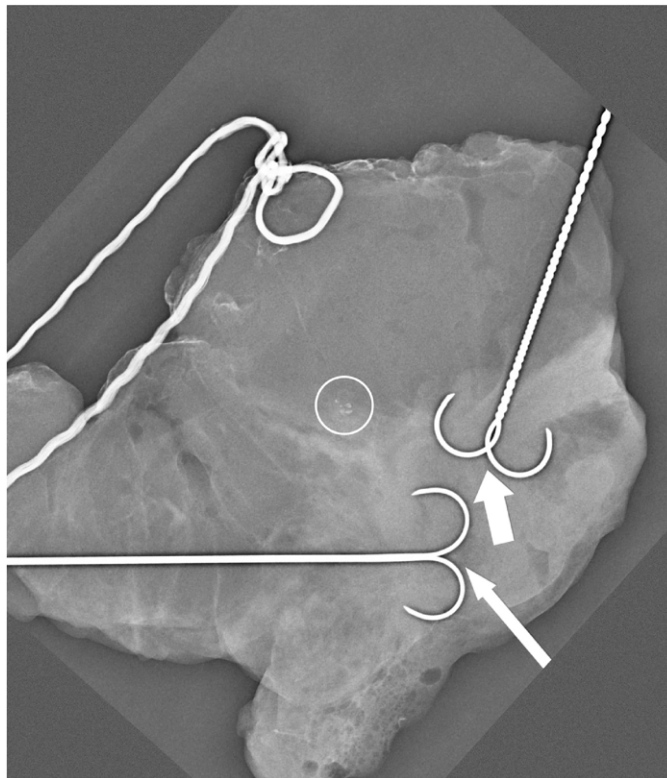
Figure 4. Specimen radiography acquired with an exposure of 0.66 mGy air-kerma: The tips of the smooth wire are directly placed in the center of tumor A (large white arrow), and those of the twisted wire directly in the center of tumor B (small white arrow). Even on specimen radiography the margins of the two breast cancers are not delineated as the cancers are situated in radiographically dense fibroglandular breast tissue. Some microcalcifications in surrounding tissue (circle) are visible.

two carcinomas differed in four aspects: firstly, the tumor size, tumor A being larger than tumor B; secondly, the microcalcifications with tumor A showing more abundant and larger microcalcifications than tumor B; thirdly, the pronounced tubule formation in tumor A; and fourthly the more prominent desmoplastic stromal response to tumor A compared to tumor B.

The calcium phosphate grains are clearly visible as black structures in tumor A (figures 6 and 7). Almost no grains of calcium phosphate could be found in the region of tumor B (figure 8) and in the region of breast tissue without tumor cells (figure 9).

In order to obtain information about the size distribution and number density of the grains we identified the grains of calcium phosphate by applying a threshold of (40, 40, 40) in red–green–blue color space of the microscope image of figure 6. The subsequent application of a morphological opening operation (erosion with followed dilation) with a morphological structure disc of $1.15\,\mu$m size removed small contact regions between touching grains while the area of the grains extending over several pixels was kept. The resulting average edge length of the grains thus was slightly smaller compared to the original distribution. For each grain the center of gravity of the pixels above threshold was determined and the radius of the circle with equivalent area to the grain area was calculated. We obtained the distribution of the thus-given radii of grains shown in figure 10 in a circular region of interest of 6 mm diameter centered in tumor A. The two-dimensional density distribution of the grains was fitted with
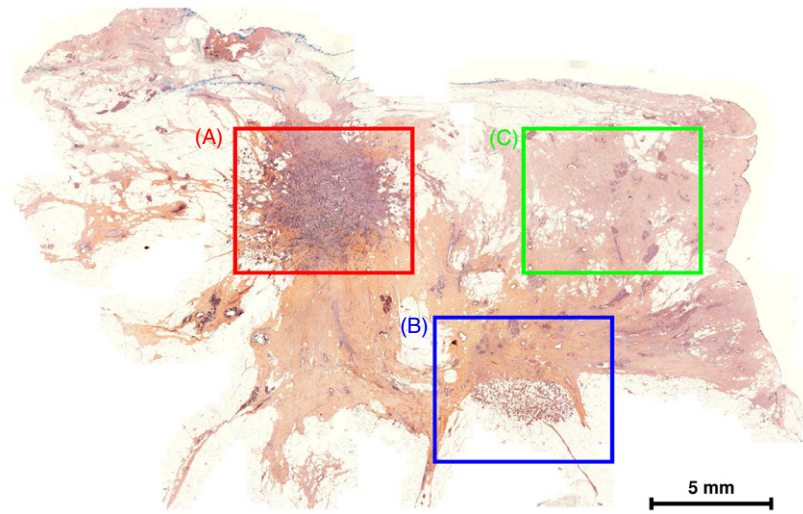
Figure 5. Microscope image of the von Kossa stained histological section from the top of lamella 3. The red rectangle frames the region of tumor A, the blue rectangle indicates the region of tumor B, and the green rectangle borders breast tissue without tumor cells.
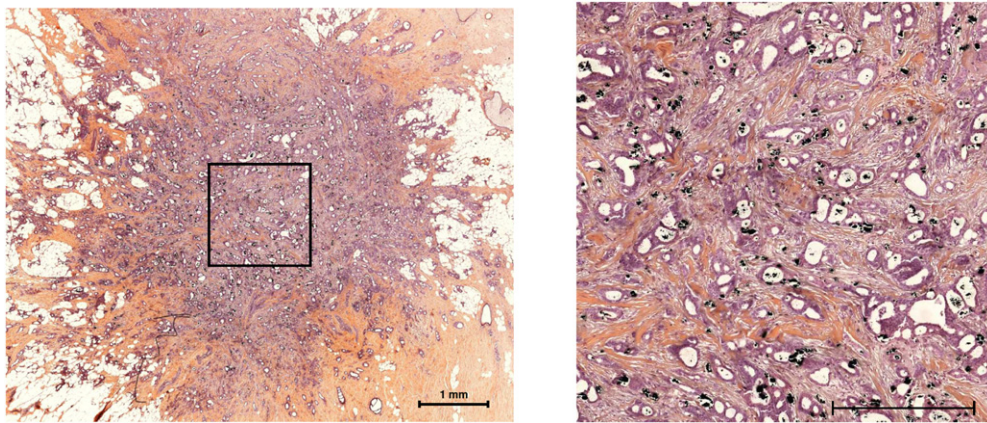

Figure 6. Microscope images of tumor A in the von Kossa stained histological section at two different magnifications. Grains of calcium phosphate are clearly visible as black dots in the right hand side image. Tubule formation is also visible. The horizontal bar indicates a length of 1 mm.

a two-dimensional Gaussian profile. For the local calcium phosphate grain number density $N(x, y)$ (number of grains per area) in tumor A at a position (x, y) in the histological section we obtained:

$$N(x, y) = N_0 \cdot e^{-\frac{(x-x_0)^2}{2\sigma_x^2}} \cdot e^{-\frac{(y-y_0)^2}{2\sigma_y^2}} \tag{1}$$

with $N_0 = 208.7 \, \frac{1}{\text{mm}^2}$, $\sigma_x = (2.10 \pm 0.15)$ mm, $\sigma_y = (2.09 \pm 0.16)$ mm and (x_0, y_0) being the center of gravity of the grain distribution in the histological section.

The distribution of radii in combination with the information on the calcium phosphate grain number density was used as input to a simulation of the attenuation and dark-field images of the interferometer.
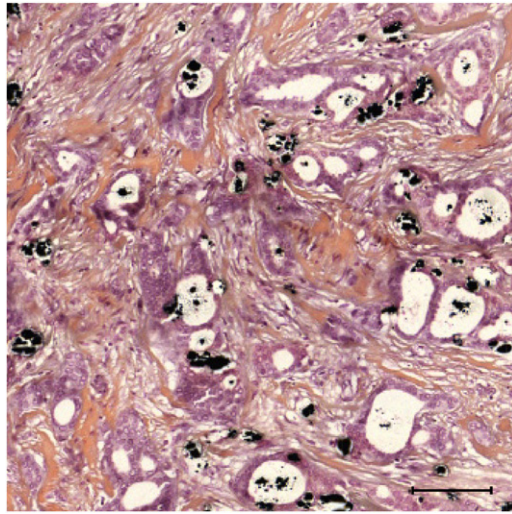
Figure 7. High magnification image of a region with calcium phosphate grains in tumor A. The horizontal bar represents $100\,\mu$m.
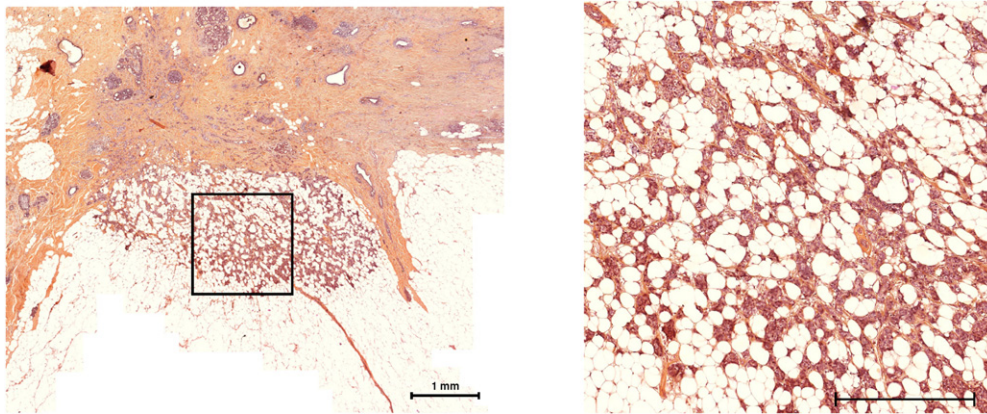

Figure 8. Microscope images of tumor B in the von Kossa stained histological section with two different magnifications. Only a few, very sparsely distributed calcium phosphate grains with sizes between 1 and $6\,\mu$m were present. The tumor showed solid growth. The horizontal bars represent a length of 1 mm.

4. Measurements with the Talbot–Lau interferometer

The x-ray tube with tungsten anode was operated at 40 kV with a current of 60 mA. With no object in the beam we obtained a maximum visibility of 24.4% and an average visibility of 20.7% in the common projection area of the three gratings. The gratings cover a common imaging area of 24.14 mm × 13.27 mm, which is smaller than the sample area. Thus it was necessary to perform separate phase-contrast measurements for different parts of the object. The object has been covered completely using 2×4 phase-contrast measurements each with eight phase-steps over two periods of the G2 analyzer grating.

For each pixel the measured intensity $I(x)$ as a function of the G2 position x was fitted by $I_0(x) = a_0 + b_0 \sin(\tilde{k}x + \varphi_0)$ with $\tilde{k} = 2\pi/p_2$ for the measurement without the sample and $I(x) = a + b \sin(\tilde{k}x + \varphi)$ for the measurement with the sample in the beam. The average
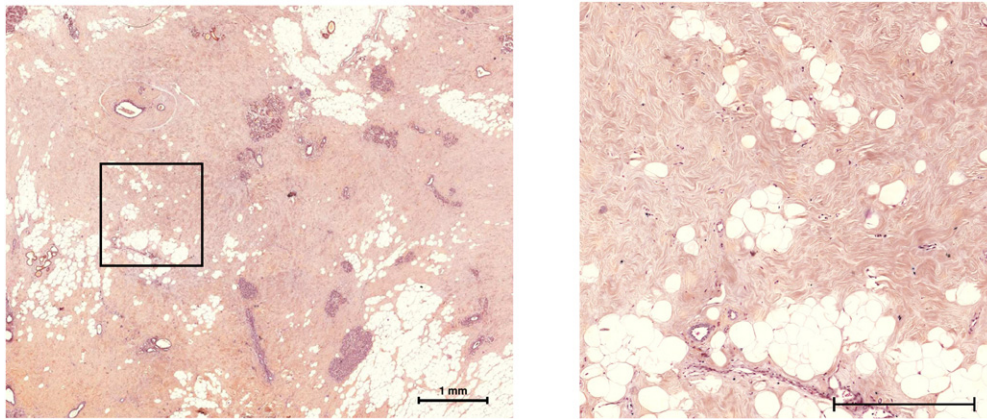
Figure 9. Microscope images of the region without tumor cells in the von Kossa stained histological section. No calcium phosphate grains are visible. The horizontal bar represents a length of 1 mm.
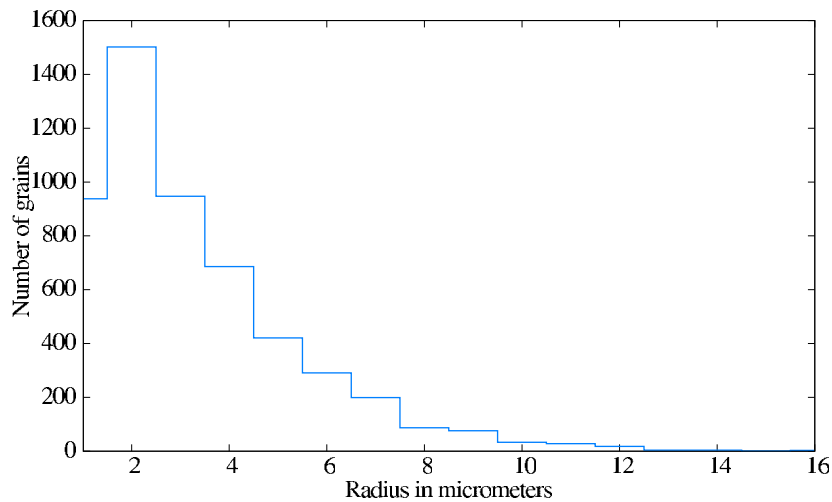

Figure 10. Distribution of the radii of circles with the same area as the calcium phosphate grains found in the histological section of tumor A.

attenuation coefficient integrated over the beam paths in the sample in front of the pixel is the information which is displayed in the so-called attenuation image. It is calculated as $A = -\ln\left(\frac{a}{a_0}\right)$. The differential phase shift is determined by $\varphi = \varphi - \varphi_0$ and the visibility as $V_0 = b_0/a_0$ for the reference measurement and $V = b/a$ for the measurement with the sample. The dark-field signal is calculated as $D = -\ln(V/V_0) = -\ln\left(\frac{b}{b_0} \cdot \frac{a_0}{a}\right)$. For each segment of the sample, three images (1 s acquisition time for each image) for each phase-step were acquired. The following analysis is based on data obtained with the subset of one image per phase-step which corresponds to an equivalent image relevant exposure of 0.85 mGy air-kerma for the complete phase-stepping. Data obtained with the full exposure of 2.55 mGy air-kerma is presented in figures 14 and 16 for comparison.

Figure 11 shows the attenuation and differential phase image of the sample obtained with an air-kerma of 0.85 mGy. None of the tumors are visible in the attenuation or the differential phase image. Figure 12 shows the average line profile of the attenuation signals of pixels between the white lines. The Weber contrast of the attenuation signals between an
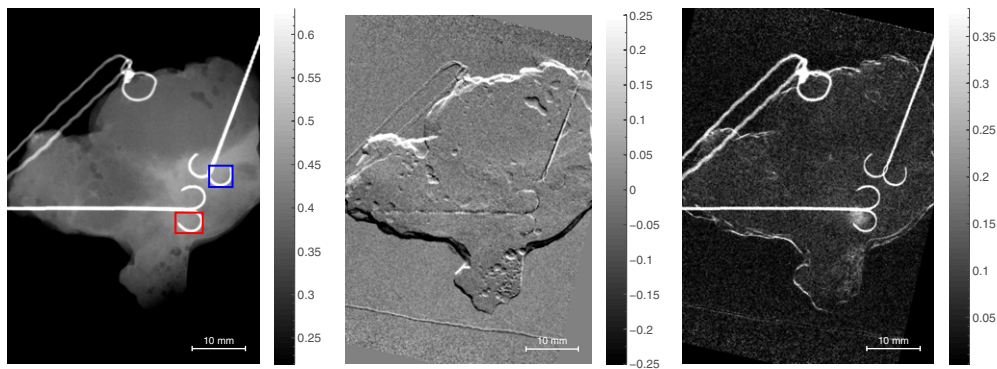
Figure 11. Attenuation (left hand side), differential phase (center) and dark-field image (right hand side) of the sample obtained with the Talbot–Lau interferometer at 0.85 mGy air-kerma. The gray scales encode attenuation signal A, differential phase signal $\varphi - \varphi_0$ in radians and dark-field signal D. The red rectangle marks tumor A, the blue rectangle borders tumor B.
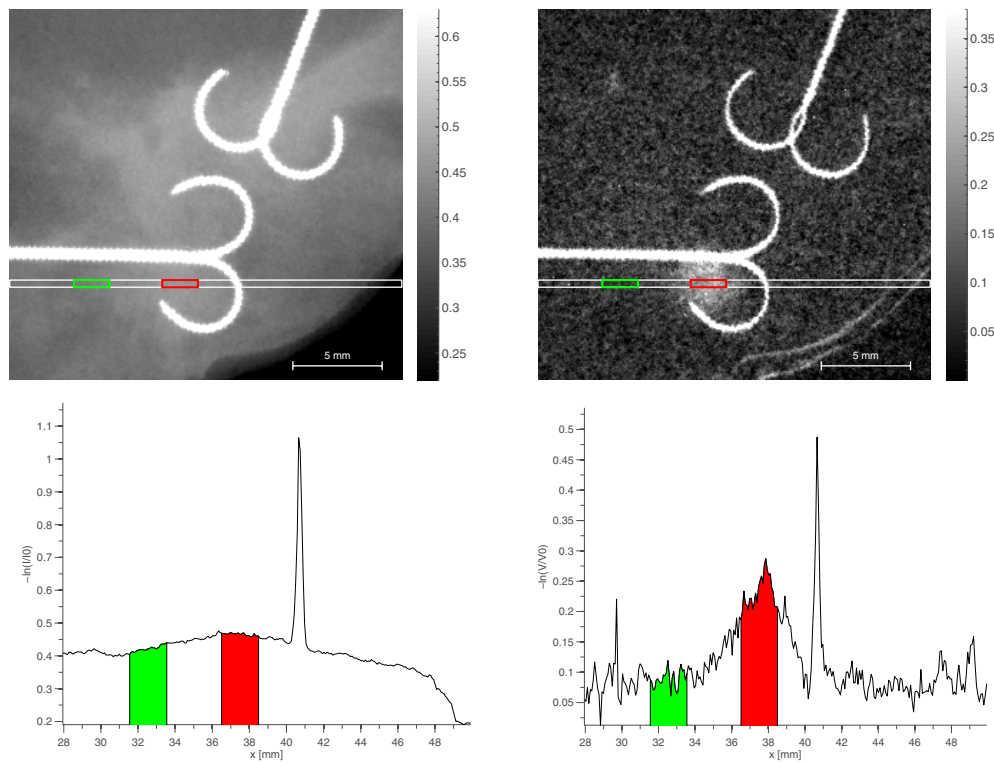

Figure 12. Top: attenuation (left hand side) and dark-field image (right hand side) in the vicinity of the tumors. Rectangles mark regions in tumor A (red) and adjacent tissue (green). The gray scales indicate attenuation signal A or the dark-field signal D. Bottom: the average line profile of the attenuation signal A (left hand side) and the dark-field signal D (right hand side) in the region of interest between the two white lines defined in the images. The spikes in the profiles are produced by the needle.
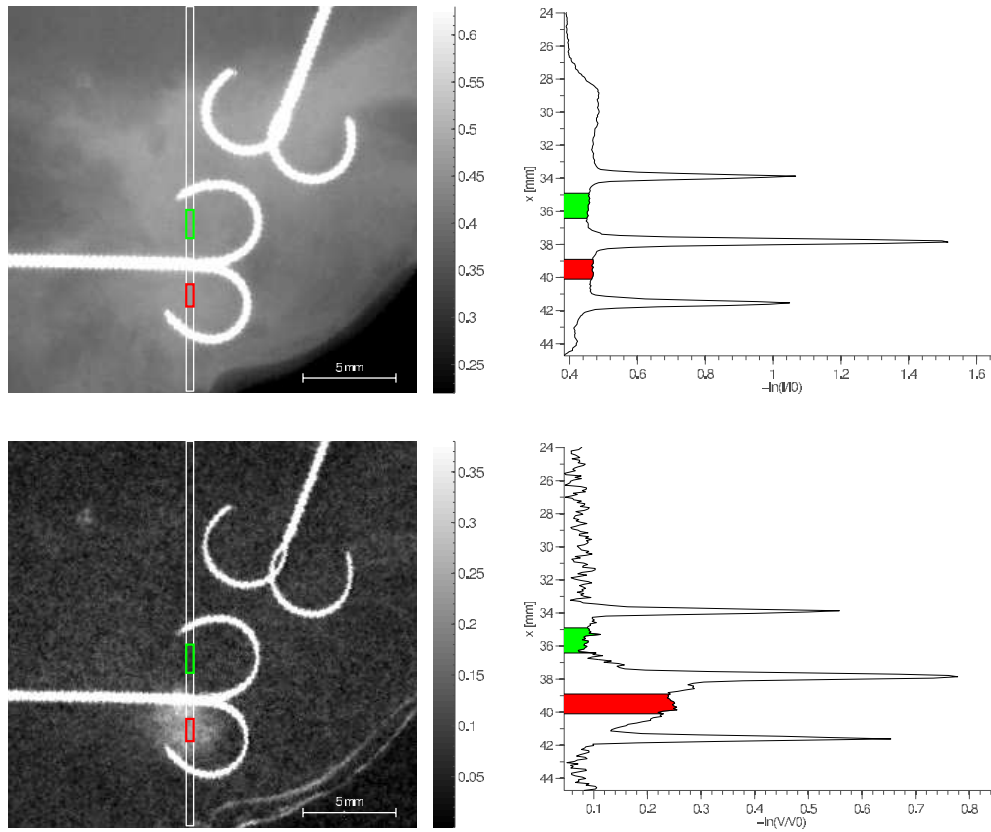
Figure 13. Regions of interest (red: tumor A with calcium phosphate grains, green: adjacent to tumor A without calcification grains) and average line profile between the white lines in a direction perpendicular to the profiles in figure 12 of attenuation (top) and dark-field signal (bottom). Again, a significant Weber contrast is apparent for tumor A in the dark-field, but not in the attenuation image.

area of interest in tumor A (red) and a region of interest in the surrounding tissue (green) was calculated to be $C_A^{\text{Weber}} = (A_{\text{tumor}} - A_{\text{surrounding}})/A_{\text{surrounding}} = 0.10$. Thus, tumor A produced an attenuation signal that was comparable to the attenuation signal of the dense tissue surrounding it. This contrast is not sufficient to highlight the tumor region because of fluctuations of the attenuation signal present all over the sample due to tissue inhomogeneities.

In contrast to this, tumor A generated a strong dark-field signal of up to 0.26 in its center, making it clearly visible in the dark-field image (figure 11 right hand side).

Figure 12 also shows the line profile of the dark-field signal for the pixels between the white lines. The Weber contrast in the marked regions of figure 12 amounts to $C_D^{\text{Weber}} = (D_{\text{tumor}} - D_{\text{surrounding}})/D_{\text{surrounding}} = 1.60$ which is much larger than the attenuation Weber contrast. Thus, tumor A produced a much stronger dark-field signal than the dense tissue surrounding it. Tumor B, where only few calcium phosphate grains were found, did not produce a significant dark-field signal.

Figure 13 shows the regions of interest (red: tumor A, green: normal tissue) and the corresponding average line profiles in a direction perpendicular to the direction of the profiles in figure 12 for the dark-field and the attenuation image. The Weber contrasts $C_D^{\text{Weber}} = 1.38$ and $C_A^{\text{Weber}} = 0.02$ reflect again that tumor A is visible in the dark-field, but not visible in the attenuation image.
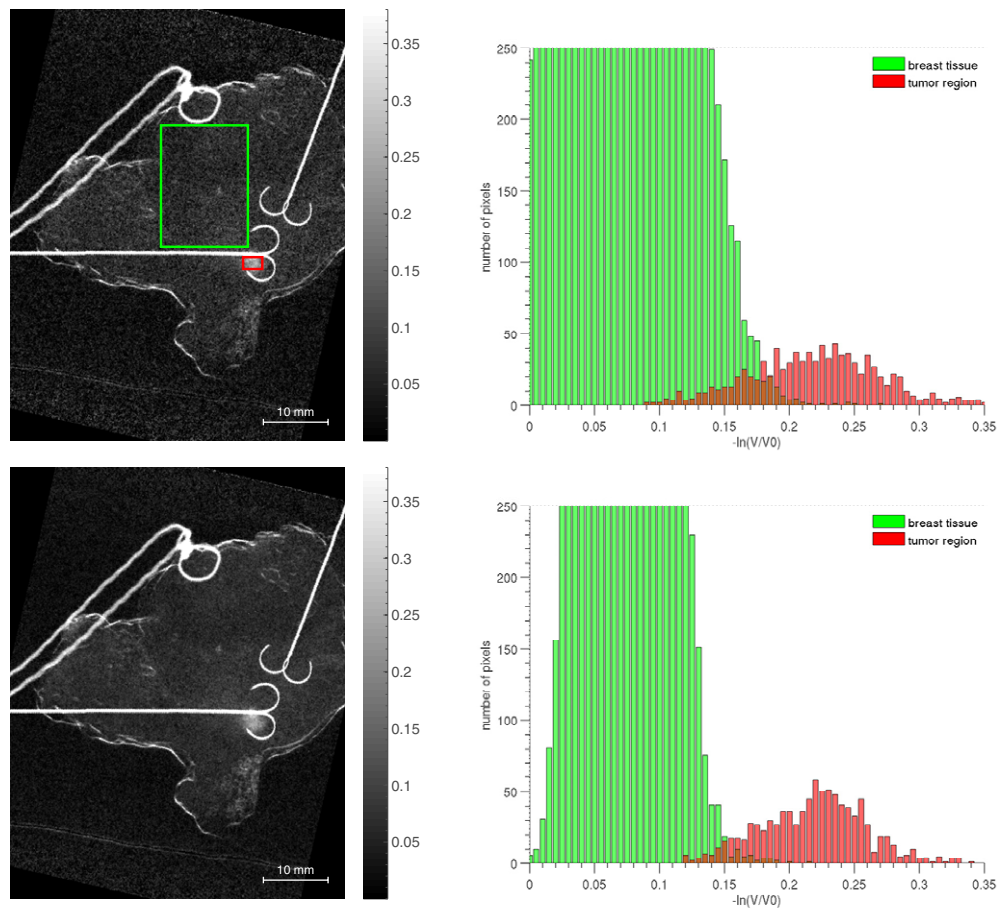
Figure 14. Dark-field images (left hand side) for 0.85 mGy air-kerma (top) and 2.55 mGy air-kerma (bottom) and corresponding distributions of dark-field signal values in the pixels of the surrounding tissue (green) and tumor A (red).

We therefore formulate the hypothesis that the distribution of calcium phosphate grains with sizes much smaller than the pixel size produced a significant dark-field signal and did not produce sufficient attenuation contrast due to the inhomogeneity of the surrounding tissue. Here, the visibility of the tumor is not limited by the contrast-to-noise ratio, but by the contrast produced by structures in the breast like glandular tissue. In order to prove this finding, figure 14 shows the dark-field images and the corresponding distribution of dark-field values for the pixels in surrounding tissue (green) and for the area of tumor A (red) for exposures of 0.85 mGy (top) and 2.55 mGy (bottom). The dark-field values in the region of tumor A are almost separated from the dark-field values of surrounding tissue at 0.85 mGy and well separated at 2.55 mGy. In contrast to this the corresponding distribution of attenuation signals of tumor A vanishes in the background caused by surrounding tissue (see figure 15).

Figure 16 shows the line profile in the dark-field image obtained with an exposure of 0.85 mGy air-kerma in comparison to the profile obtained with the full exposure of 2.55 mGy air-kerma. This indicates that—at the reduced dose level—a substantial part of the noise in the dark-field image is due to quantum noise and not only due to structures in tissue.
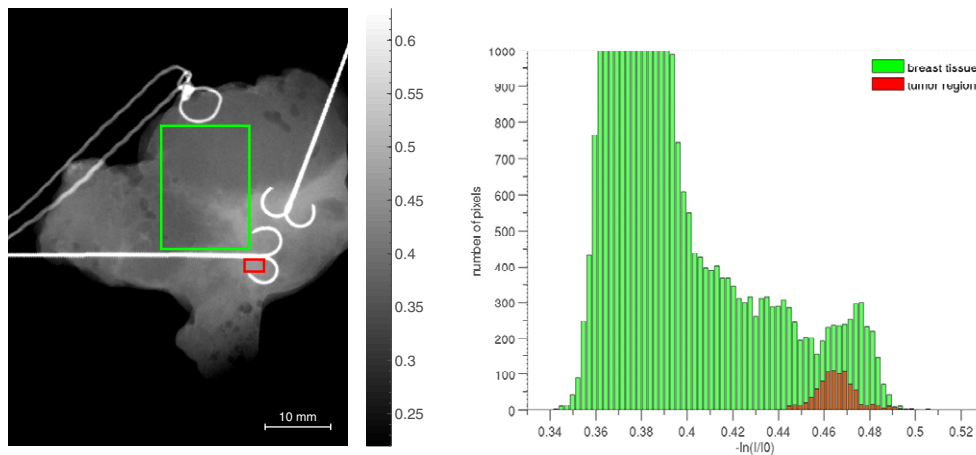
Figure 15. Left hand side: attenuation image with two regions of interest in surrounding tissue (green) and tumor A (red). Right hand side: distribution of attenuation signal values in the pixels of the two regions of interest.
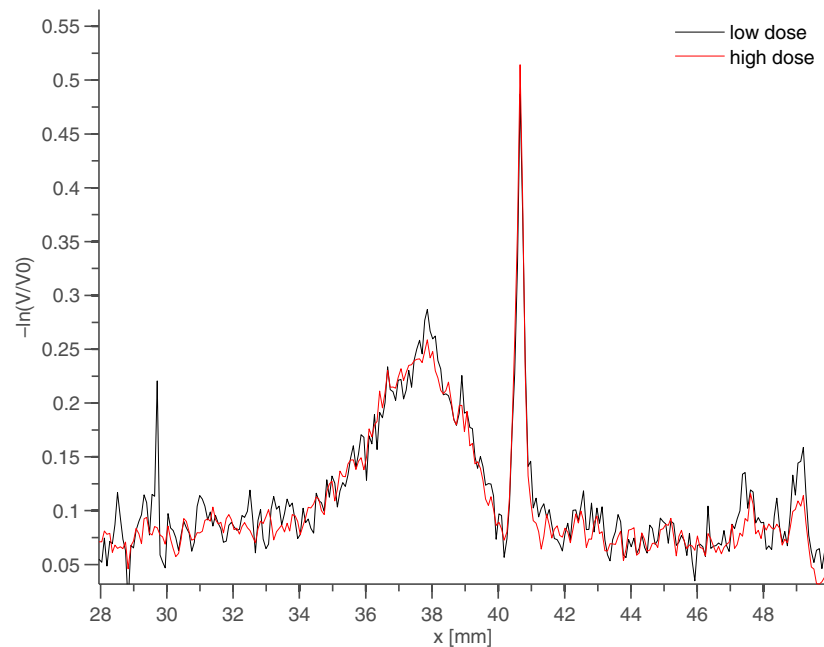

Figure 16. Average line profile (between the white lines defined in figure 12) for an exposure of 0.85 mGy air-kerma (low dose) and 2.55 mGy air-kerma (high dose).

In order to test the hypothesis we carried out a simulation of the dark-field signal generated by the distribution of apatite grains embedded in breast tissue.

5. Simulation of the dark-field signal

Malecki *et al* (2012) recently presented an x-ray wave-propagation simulation program. Their simulation results of the dark-field signal in a Talbot–Lau-interferometer are in agreement with

the predictions derived from the model presented by Lynch *et al* (2011) within the accuracy used in the simulation. The scattering objects in their study are filled spheres with radii from 1.5 to 50 μm which is comparable to the radii of the grains of calcium phosphate found in our sample.

Independent from Malecki *et al* (2012) we have developed a simulation program which numerically carries out x-ray wave propagation through the Talbot–Lau interferometer and through objects by calculating the wave function $\Psi(x)$ as a function of x on an axis perpendicular to the direction of propagation (z) and perpendicular to the direction (y) of the grating bars. Each monochromatic component of the x-ray field emitted by the x-ray tube is propagated individually through the imaging system and the sample. The intensity distributions of all propagated monochromatic waves are weighted with their relative flux in the spectrum and summed to obtain the intensity pattern of the complete wave field.

The influence of the gratings G1, G2 and the sample are calculated in the projection approximation (Morgan *et al* 2010) which means that the influence of an object comprising J materials illuminated by a wave function $\Psi_{in}(E)$ with wave number $k(E)$ is given by:

$$\psi_{out}(E) = \psi_{in}(E) \cdot \exp\left(-i\sum_{j=1}^{J} k(E)\delta_j(E)d_j\right) \cdot \exp\left(-\sum_{j=1}^{J} k(E)\beta_j(E)d_j\right) \tag{2}$$

Here, d_j is the total thickness of material j and $\delta_j(E)$ is the refractive index decrement of material j. $\beta_j(E) = \mu(E)/(2 \cdot k(E))$ represents attenuation obtained from linear attenuation coefficients[9]. Thus photoelectric absorption and Compton scattering are taken into account. The refractive index decrements of materials are calculated as a function of energy from the atomic scattering factors provided by the National Institute of Standards and Technology (NIST) (see footnote 9).

The sampling of the wave front is carried out with an accuracy perpendicular to the beam which depends on local differences in refractive index decrements and energy, but always averages the wave function in regions smaller than 100 nm, a length which is smaller than 10% of the smallest calcium phosphate grains extracted from the histological section. Free-space propagation between G1 and G2 is carried out for each monochromatic wave by convolution of the wave function with the corresponding Fresnel propagator. The structure of G0 and the extension of the focal spot are taken into account by an additional convolution with the product of the grating function and the focal spot intensity distribution, projected through G1 onto the plane of G2. The phase-stepping is emulated by calculating the influence of G2 in projection approximation taking the x-position of G2 into account. The intensity in each detector pixel for each phase-step is determined by integrating the intensity behind G2 over an area which equals the detector pixel area backprojected onto the G2-plane. The energy dependent detection efficiency of the CsI flat panel detector is also taken into account.

As the signal in the interferometer depends strongly on photon energy, we measured the emission spectrum of the x-ray tube with the photon-counting silicon pixel-detector Timepix (Llopart *et al* 2007) using the USB readout (Vykydal *et al* 2006) and the data acquisition software Pixelman (Holy *et al* 2006). A pixelwise calibration of the discriminator thresholds was performed (Sievers *et al* 2012). For each pixel the number of counts as a function of discriminator threshold was measured in the interferometer at a x-ray tube voltage of 40 kV. The sampled spectrum of emitted x-ray energies $\{S_i\}$ was calculated from the measured spectrum of deposited energies $\{M_k\}$ and the response matrix $\{R_{ki}\}$ by Bayesian deconvolution:

$$S_i^{n+1} = \frac{1}{\tau_i} S_i^n \sum_k \frac{R_{ki} \cdot M_k}{\sum_j R_{kj} \cdot S_j^n}, \tag{3}$$
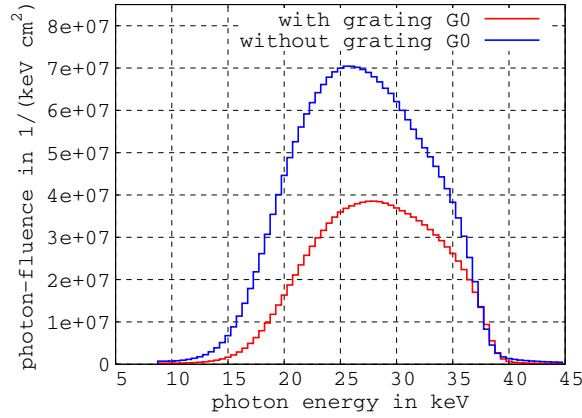
---

[9] www.nist.gov.

Figure 17. Measured x-ray spectra without (blue line) and with (red line) G0 determined with the Timepix detector. The impact of the grating G0 on the spectrum is clearly visible: the photon flux is reduced by a factor of ≈ 2 and the spectrum is hardened.

with the iteration index n and the mean number of triggered pixels per incident photon $\tau_i = \sum_k R_{ki}$. i, k, j denote the energy channel index of either the measurement $\{M_k\}$ or the impinging spectrum $\{S_i\}$. The matrix $\{R_{ki}\}$ represents the simulated detector response to monoenergetic irradiation. More details can be found in Sievers *et al* (2012). The resulting emission spectrum of the tube is shown in figure 17 and is used as input to the simulation.

In order to validate the wave-field simulation we carried out a simulation of the dark-field signal generated by hydroxylapatite spheres with a radius of $5\,\mu$m embedded in a 1.5 mm thick layer of breast tissue specified in ICRU 46 (breast mammary gland tissue, adult 3) in the 25 keV design energy Talbot–Lau setup with G2 being positioned in the first fractional Talbot distance given by $d_T = p_1^2/8/\lambda_{\text{design}}$ behind G1. The results were compared with the dark-field signal calculated with the analytical model presented by Yashiro *et al* (2010) (equation (5)). The relative volume density of hydroxylapatite in breast tissue has been set to 10% in order to achieve a large dynamic range in the dark-field signal in the energy range of interest. Figure 18 shows the results of the wave-field simulation in comparison with the results of the analytical model given in Yashiro *et al* (2010). Deviations are smaller than 10%. In general the signal generated by the wave-field simulation is smaller than the value calculated with the analytical model.

We then performed a simulation of tumor A in the sample. The calcium phosphate grains were modeled as circular structures of hydroxylapatite ($Ca_5[OH|(PO_4)_3]$) which is a common form of calcium phosphate in the human body. Additionally we assumed that the mass density of the grain material equaled the density of crystalline hydroxylapatite ($\rho = 3.16$ g cm^{-3}) which leads to maximum dark-field values for this material. The grains were distributed in the (x, z)-plane and their radii followed the extracted distribution from the histological section shown in figure 10. We assumed that the distribution of radii did not vary with position. The hydroxylapatite circles were embedded with locally varying number density in a breast tissue slice of 4.7 mm thickness in the beam direction. The chemical composition of breast tissue was taken as specified in ICRU 46 (breast mammary gland tissue, adult 3). In order to take the stronger attenuation in the surroundings of tumor A (see left hand side of figure 11) into account the breast tissue density in tumor A was increased by 11.7 % compared to ICRU 46 data so that the attenuation signal of tissue directly adjacent to and in tumor A was reproduced with the simulation.
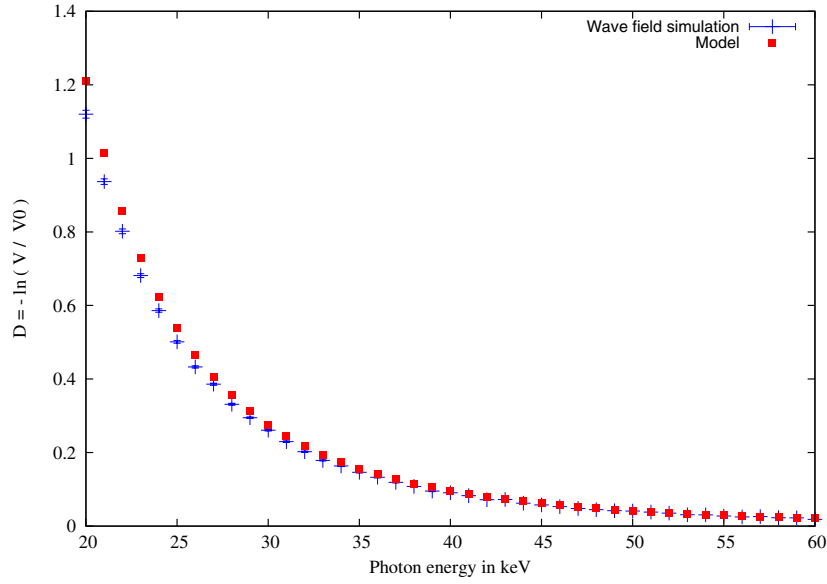
Figure 18. Comparison between dark-field signal obtained with the wave-field simulation (blue) and with the model (red) presented in Yashiro *et al* (2010).

In order to determine the *z*-dependence (beam direction) of the three-dimensional calcium phosphate grain number density in tumor A, we performed a phase-contrast computed-tomography measurement with the paraffin-embedded sample. The rotation axis of the paraffin fixed sample was oriented perpendicular to the histological section. The thickness of the sample in the beam direction was measured to be 4.7 mm. Filtered backprojection of the dark-field signal with the Ram–Lak filter kernel was performed. A line profile in the dark-field volume data perpendicular to the histological section (*z*-axis) through the center of the tumor A was extracted. The *z*-position of the histological section was set to $z = 0$ mm. The *z*-dependence of the measured profile could be described by a Gaussian with standard deviation $\sigma_z = (1.02 \pm 0.19)$ mm centered at $z_0 = -0.77$ mm.

This method to extract the *z*-dependence of the number density of grains from dark-field volume data reconstructed using filtered backprojection (Bech *et al* 2010) is justified because the variance on the phase front of a wave with wavelength λ passing a sample with thickness d containing a distribution of small-scale scatterers with number volume density N and radius a is given by:

$$\sigma^2 = (Nd)\pi a^2 (\Delta\rho)^2 r_e^2 \lambda^2 (2a^2) \tag{4}$$

with the classical electron radius r_e and the electron-density difference $\Delta\rho$ (Yashiro *et al* 2010). The dark-field signal, defined in our case as $D = -\ln(V/V_0)$, can therefore be approximated by

$$D \approx \sigma^2 (1 - \gamma) \approx Nd\pi a^2 (\Delta\rho)^2 r_e^2 \lambda^2 (2a^2)(1 - \gamma) \tag{5}$$

where γ depends on the shape of the scatterers, the interferometer setup and the wavelength, but not on the amount of scatterers.

Due to the fact that $\sigma_x \approx \sigma_y$ the two dimensional number density $N_{\text{sample}}(x, z)$ of the calcium phosphate grains within the sample in every slice through tumor A which contains the *z*-axis (beam direction) could be modeled as:
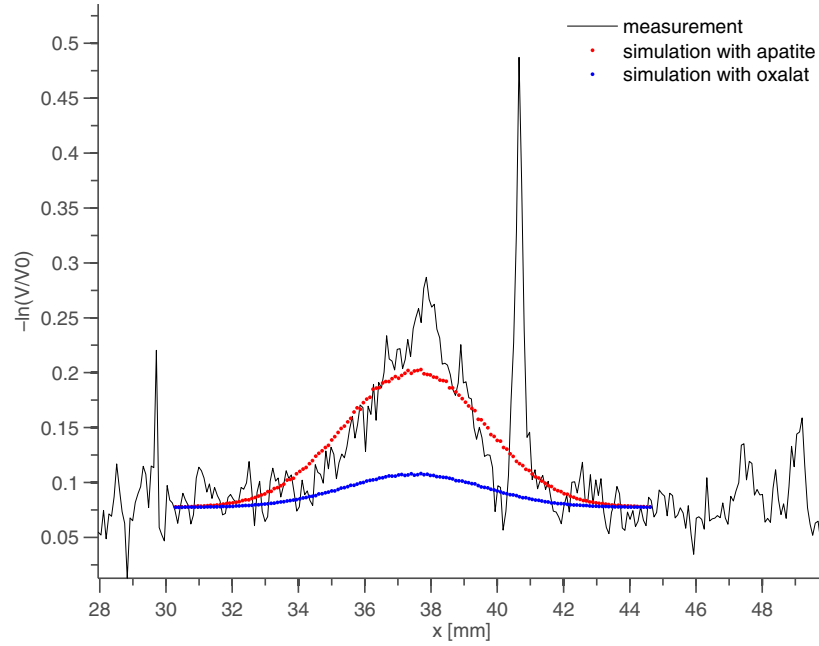
Figure 19. Simulated dark-field line profile in comparison to a measured line profile through the center of the tumor as shown in figure 12.

$$N_{\text{sample}}(x, z) = 277.6 \cdot e^{-\frac{x^2}{2\sigma_x^2}} \cdot e^{-\frac{(z-z_0)^2}{2\sigma_z^2}} \frac{1}{\text{mm}^2}. \tag{6}$$

The simulation of the dark-field signal generated in tumor A was carried out for 1024 different realizations of locations according to equation (6) and individual radii according to figure 10 of the grains. The dark-field signal along the *x*-axis was calculated for each realization. The average dark-field signal generated by breast tissue without the tumors was extracted from the measurement and added to the simulated dark-field signal of the embedded grains. The resulting simulated expectation value for the dark-field signal along the *x*-axis through the center of tumor A is shown in figure 19 in comparison to the measured line profile. It can clearly be seen that the distribution of hydroxylapatite grains can indeed reproduce the dark-field signal observed in tumor A to a substantial part. The remaining discrepancies might have their origin in deviations of the local calcium phosphate grain density from the adapted Gaussian profile or deviations of the radii of the grains to the radius distribution determined with the histological section.

The calcium phosphate grains in tumor B were very inhomogeneously distributed. No grain at all could be found in more than half of non-overlapping microscope views. A local cluster with four grains with a maximum radius of 4.5 μm in one microscope view with 0.3 mm^2 area was found. If one takes a dilution factor of 50% due to the inhomogeneous distribution of the grain clusters into account one can estimate a maximum grain number density of $N_{0,\text{B}} = 6.7 \frac{1}{\text{mm}^2}$ in tumor B. The expected maximum dark-field signal generated by the calcium phosphate grains in tumor B can then be estimated by scaling the maximum of the simulated dark-field signal produced by the grains in tumor A with the ratio of the grain number densities of both tumors. A maximum dark-field signal of 0.076 generated by the calcium phosphate grains and the breast tissue layer for tumor B is obtained. Such a small signal vanishes in the dark-field background signal produced by breast tissue (see figure 14). Tumor B is invisible in the dark-field image.

The attenuation Weber contrast was determined by the simulation to be $C_A^{\mathrm{Weber}} = (A_{\mathrm{tumor}} - A_{\mathrm{surrounding}})/A_{\mathrm{surrounding}} = 0.014$. Thus the simulation indicated that the distribution of hydroxylapatite grains did not lead to a substantial attenuation contrast. This finding agrees with the measurement and shows that indeed the dark-field signal provides additional information which is not accessible by attenuation imaging under realistic conditions.

If we now assume—in contradiction to the histopathological finding—that the calcification grains consisted of calcium oxalate (CaC_2O_4) with its maximum density of $\rho = 2.12\,\mathrm{g\,cm^{-3}}$ instead of hydroxylapatite we would have obtained a much weaker dark-field signal with the simulation. Figure 19 also shows this result. It is clearly visible that calcium oxalate, assuming the same concentration and grain sizes as hydroxylapatite, would not have been able to produce the observed strong dark-field signal. Thus, the sensitivity of the dark-field to hydroxylapatite is significantly larger than the sensitivity to calcium oxalate.

6. Summary and conclusion

We have shown that certain invasive breast carcinomas can produce a dark-field contrast but no attenuation contrast, neither in a Talbot–Lau interferometer with 25 keV design energy nor in clinical mammography at standard dose levels.

We investigated a resection specimen with two invasive ductal carcinomas. A histological section through the tumor region revealed that one of the tumors contained grains of a calcium phosphate with sizes between 1 and 40 μm with a number density of up to $208.7\,\frac{1}{\mathrm{mm^2}}$ in a histological section in the center of the tumor.

A possible explanation of the origin of the dark-field signal has been strengthened with a wave-field simulation. We performed a wave field simulation to calculate the dark-field image of the histologically determined size and density distribution of hydroxylapatite grains embedded in breast tissue. The calculated dark-field signal and the measured dark-field with the Talbot–Lau imaging set-up are then in agreement. Also the calculated attenuation signals show very low contrast which would explain that the tumor is not visible in attenuation images. Given the number density and distribution of grain sizes, it is shown that calcium oxalate would have produced a much weaker dark-field signal.

With our investigations and the presented results we open the window to an analysis of Talbot–Lau dark-field images for medical applications. The clinical relevance of these findings is not clear up to now and shall be subject to further studies. Nevertheless, our findings are strong arguments that strengthen the importance of x-ray phase contrast imaging in combination with standard x-ray tubes.

Acknowledgments

[10] The described functionality is work-in-progress and commercially not available.

References

Ando M *et al* 2005 Attempt at visualizing breast cancer with x-ray dark field imaging *Japan. J. Appl. Phys.* **44** L528–31

Anton G *et al* 2013 Grating-based darkfield imaging of human breast tissue *Z. Med. Phys.* at press (doi:10.1016/j.zemedi.2013.01.001)

Arfelli F *et al* 2000 Mammography with synchrotron radiation: phase-detection techniques *Radiology* **215** 286–93

Bech M, Bunk O, Donath T, Feidenhans'l R, David C and Pfeiffer F 2010 Quantitative x-ray dark-field computed tomography *Phys. Med. Biol.* **55** 5529–39

Castelli E *et al* 2011 Mammography with synchrotron radiation: first clinical experience with phase-detection technique *Radiology* **259** 684–94

Cong W, Pfeiffer F, Bech M and Wang G 2011 X-ray dark-field imaging modeling *J. Opt. Soc. Am.* A **29** 908–12

Endo T *et al* 2011 Development of a new breast imaging method based on x-ray Talbot–Lau interferometry *RSNA 2011: 97th Science Assembly and Annual Meeting of Radiological Society of North America (McCormick Place, Chicago, IL, 27 Nov.–2 Dec.)* SSC15-09

Herzen J, Donath T, Pfeiffer F, Bunk O, Padeste C, Beckmann F, Schreyer A and David C 2009 Quantitative phase-contrast tomography of a liquid phantom using a conventional x-ray tube source *Opt. Express* **17** 10010

Holy T, Jakubek J, Pospisil S, Uher J, Vavrik D and Vykydal Z 2006 Data acquisition and processing software package for Medipix2 *Nucl. Instrum. Methods Phys. Res.* A **563** 254

Kenntner J, Altapova V, Grund T, Pantenburg F J, Meiser J, Baumbach T and Mohr J 2012 Fabrication and characterization of analyzer gratings with high aspect ratios for phase contrast imaging using a Talbot interferometer *AIP Conf. Proc.* **1437** 89–93

Keyriläinen J, Fernández M, Fiedler S, Bravin A, Karjalainen-Lindsberg M, Virkkunen P, Elo E, Tenhunen M, Suortti P and Thomlinson W 2005 Visualisation of calcifications and thin collagen strands in human breast tumour specimens by the diffraction-enhanced imaging technique: a comparison with conventional mammography and histology *Eur. J. Radiol.* **53** 226–37

Kiss M Z, Sayers D E, Zhong Z, Parham C and Pisano E D 2004 Improved image contrast of calcifications in breast tissue specimens using diffraction enhanced imaging *Phys. Med. Biol.* **49** 3427–39

Llopart X, Ballabriga R, Campbell C, Heijne E H M, Tlustos L and Wong W 2007 Timepix, a 65k quantum imager readout chip for arrival time, energy and/or event counting measurements *Nucl. Instrum. Methods Phys. Res.* A **581** 485–94

Lynch S K, Pai V, Auxier J, Stein A F, Bennett E E, Kemble C K, Xiao X, Lee W K, Morgan N Y and Wen H H 2011 Interpretation of dark-field contrast and particle-size selectivity in grating interferometers *Appl. Opt.* **50** 4310–19

Malecki A, Potdevin G and Pfeiffer F 2012 Quantitative wave-optical numerical analysis of the dark-field signal in grating-based x-ray interferometry *Europhys. Lett.* **99** 48001

Morgan K S, Siu K K and Paganin D M 2010 The projection approximation and edge contrast for x-ray propagation-based phase contrast imaging of a cylindrical edge *Opt. Express* **18** 9865–78

Pfeiffer F, Bech M, Bunk O, Kraft P, Eikenberry E F, Brönnimann C, Grünzweig C and David C 2008 Hard-x-ray dark-field imaging using a grating interferometer *Nature Mater.* **7** 134–7

Pfeiffer F, Weitkamp T, Bunk O and David C 2006 Phase retrieval and differential phase-contrast imaging with low-brilliance x-ray sources *Nature Phys.* **2** 258–61

Rigon L, Arfelli F and Menk R H 2007 Three-image diffraction enhanced imaging algorithm to extract absorption, refraction, and ultrasmall-angle scattering *Appl. Phys. Lett.* **90** 114102

Schulz-Wendtland R, Fuchsjäger M, Wacker T and Hermann K P 2009 Digital mammography: an update *Eur. J. Radiol.* **72** 258–65

Sievers P, Klammer J, Michel T, Hupe O and Anton G 2012 Improving the spectral resolution of a highly pixelated detector by applying a pixel-by-pixel energy calibration for investigating the spectral properties of the anode heel effect *J. Instrum.* **7** P07011

Sievers P, Weber T, Michel T, Klammer J, Büermann L and Anton G 2012 Bayesian deconvolution as a method for the spectroscopy of x-rays with highly pixelated photon counting detectors *J. Instrum.* **7** P03003

Stampanoni M, Wang Z, Thüring T, David C, Roessl E, Trippel M, Kubik-Huch R A, Singer G, Hohl M and Hauser N 2011 The first analysis and clinical evaluation of native breast tissue using differential phase-contrast mammography *Invest. Radiol.* **46** 801–6

Vykydal Z, Jakubek J and Pospisil S 2006 USB interface for Medipix2 pixel device enabling energy and position-sensitive detection of heavy charged particles *Nucl. Instrum. Methods Phys. Res.* A **563** 112

Yashiro W, Terui Y, Kawabata K and Momose A 2010 On the origin of visibility contrast in x-ray Talbot interferometry *Opt. Express* **18** 16890–901